frontiers in Materials

ORIGINAL RESEARCH
published: 10 December 2019
doi: 10.3389/fmats.2019.00322

The Poisoning Effect of Al and Be on Mg—1 wt.% Zr Alloy and the Role of Ultrasonic Treatment on Grain Refinement

*Nagasivamuni Balasubramani, Gui Wang, David H. StJohn and Matthew S. Dargusch**

Centre for Advanced Materials Processing and Manufacturing (AMPAM), School of Mechanical and Mining Engineering, The University of Queensland, St. Lucia, QLD, Australia

Addition of Al—Be master alloy to a Mg—Zr alloy reduces melt oxidation, however, it has a detrimental grain coarsening effect that is believed to be caused by an unknown interaction of Be with the Zr nucleant particles. However, this study found that Al is the major cause of grain coarsening. By analysis of intermetallic phases and chemical analysis for solute Zr, it was revealed that Al reacts with the undissolved α–Zr particles forming Zr—Al intermetallic phases and reducing the amount of solute Zr both of which lead to a decrease in the grain refinement efficiency of the master alloy. Despite this negative effect of Al on grain refinement, application of ultrasonic treatment (UST) produces significant grain refinement of the Mg—Zr—Al—Be alloy demonstrating the potential for developing ignition-proof and grain refined Mg alloys.

Keywords: grain refinement, ultrasonic treatment, Mg—Zr alloy, Al—Be master alloy, nucleant poisoning

OPEN ACCESS

Edited by:
John L. Provis, University of Sheffield, United Kingdom

Reviewed by:
Wenxiang Xu, Hohai University, China
Feng Wang, Brunel University London, United Kingdom

****Correspondence:***
Matthew S. Dargusch
m.dargusch@uq.edu.au

Specialty section:
This article was submitted to Structural Materials, a section of the journal Frontiers in Materials

Received: *24 May 2019*
Accepted: *22 November 2019*
Published: *10 December 2019*

Citation:
Balasubramani N, Wang G, StJohn DH and Dargusch MS (2019) The Poisoning Effect of Al and Be on Mg—1 wt.% Zr Alloy and the Role of Ultrasonic Treatment on Grain Refinement. Front. Mater. 6:322. doi: 10.3389/fmats.2019.00322

INTRODUCTION

Ultrasonic treatment (UST) applied during alloy solidification produces excellent grain refinement which is necessary to achieve improved mechanical properties of the alloys (StJohn et al., 2005, 2013; Eskin, 2014, 2017). This attractive feature of UST facilitates opportunities to explore new alloy systems for which an appropriate grain refiner is unavailable (Nagasivamuni et al., 2018). Significant grain refinement has been reported for pure metals (Nagasivamuni et al., 2018, 2019b), binary alloys without refiners (Qian et al., 2010; Srivastava et al., 2017; Wang et al., 2017b) and in the presence of potent grain refiners (Ramirez et al., 2008; Atamanenko et al., 2010; Wang et al., 2017d; Nagasivamuni et al., 2019a). The application of UST to alloys containing elements that poison nucleation has also resulted in improved refinement. For example, the exceptional grain refinement of Al alloys by the addition of Ti is poisoned by the addition of Zr (Atamanenko et al., 2010; Sreekumar and Eskin, 2016) or Si (Wang et al., 2016b). It has been reported that UST generated cavitation enhances nucleation by reducing the poisoning effect and this results in grain refinement (Atamanenko et al., 2010; Sreekumar and Eskin, 2016; Wang et al., 2016b). Similarly, in carbon inoculated commercial Mg—Al alloys the interaction of Fe or Mn with C is reported to cause poisoning of grain refinement (Easton et al., 2006; Du et al., 2010) while the application of UST results in excellent grain refinement (Ramirez et al., 2008; Nimityongskul et al., 2010).

The interaction of impurities with the added grain refiner particles are specific to the type of alloy and the grain refiner. For instance it is well-known that additions of Zr to Mg alloys that contain Al, Fe, Si (StJohn et al., 2005, 2013) is not effective in promoting

grain refinement and for Mg—Al alloys (AZ series), grain refinement by carbon inoculation is affected by the presence of Fe or Mn (StJohn et al., 2005, 2013; Easton et al., 2006; Du et al., 2010). Sometimes a complex interaction might occur in these alloys due to the formation of ternary or multi-component phases that may act as nucleant particles or degrade the nucleation potential of a potent particle (Easton et al., 2006; Du et al., 2010; Huang et al., 2010). Of all these grain refiner specific impurities, Be is an interesting element which has been reported to exhibit a poisoning effect in most of the Mg alloys (Mg—Al, Mg—RE and Mg—Zr) at trace levels of <100 ppm (i.e., 0.01 wt.%, all the compositions mentioned in this paper are in wt.%) (Cao et al., 2004). The advantage of adding Be to Mg alloys at trace levels is its tendency to reduce oxidation of the melt by the formation of a non-porous BeO + MgO oxide layer which in turn reduces the amount of greenhouse gases (such as CO_2 and SF_6) used during Mg melting and casting (Zeng et al., 2001b; Tan et al., 2016, 2018). However, the mechanism of grain coarsening and the effective methods to refine or reduce the grain coarsening tendency have not been reported for Mg alloys that contain trace amounts of Be. Investigating the application of UST to Be containing Mg-Zr alloy melts by determining the composition of dissolved solute Zr (Zr_S) and total Zr (Zr_T) by chemical analysis (Qian et al., 2003; Nagasivamuni et al., 2019a) could provide a better understanding of the underlying mechanisms behind nucleant poisoning and potentially lead to the development of grain refined Be-containing, ignition proof Mg alloys.

Therefore, the present work seeks to investigate the effect of UST on the grain refinement of Mg—1% Zr alloy with 0.01% Be by applying UST in (i) the liquid stage (Mg melt containing α-Zr particles) and (ii) during solidification (from above to below the Mg alloy liquidus temperature). This study is also focused on identifying the mechanisms responsible for poisoning the grain size.

EXPERIMENTAL PROCEDURE

Commercial purity Mg (99.91 wt.%), and Mg—25Zr and Al—5Be master alloys were used to produce Mg—1Zr alloy containing 0.01% Be under the protection of cover gas at 780°C. The use of an Al—Be master alloy is the standard practice of adding Be to commercial Mg alloys and for permanent mold castings with the maximum addition being limited to 0.01% Be (Zeng et al., 2001b; Czerwinski, 2014). The addition of the 0.01% Be from the master alloy increases the Al content of the alloy to 0.2%, therefore, in this study this alloy is referred to as a Mg—1Zr—AlBe alloy. Approximately 220–240 g of Mg was melted in a boron nitride coated clay-graphite crucible. Master alloys containing Zr and Be were added to the Mg melt together and there was no significant time difference between the addition of master alloys. The melt was stirred for 2 min and then removed from the furnace after 5 min to solidify in room temperature atmosphere for the as-cast condition. UST applied above the liquidus temperature of the Mg alloy for 1 min is referred to as UST-L (750 until 660°C) and during solidification is referred to as UST-S (690–650°C) applied for 2 min. Additional details on the methods adopted and equipment used during the casting process, UST, sample preparation, composition analysis for solute (Zr_S) and total Zr (Zr_T) and etching procedures are described elsewhere (Nagasivamuni et al., 2019a,b). **Table 1** shows the composition of the alloys investigated in the as-cast condition and after UST. All the chemical analysis samples were taken from the top region of the casting and for the as-cast alloy the composition was also analyzed from the bottom region of the sample that contains settled α-Zr particles as shown in **Figure 1A**. A Hitachi table top scanning electron microscope (TM3030) equipped with Energy Dispersive X-ray spectroscopy (EDS) at an accelerating voltage of 15keV and Bruker D8 Advance MKII X-ray diffraction were used to characterize the nucleant particles in the alloy.

RESULTS

Figures 1A–C show the macrostructures of the Mg—1Zr—AlBe alloy in the as-cast, UST-L and UST-S conditions and their respective microstructures are shown in **Figures 1D–F**. For comparison, the macro and micro structures of the Mg—1Zr alloy cast under similar conditions are shown in **Figures 1G–I** (Nagasivamuni et al., 2019a). **Figure 1D** exhibits a coarse microstructure with a smaller number of particles in the matrix due to settling of α-Zr particles to the bottom region of the casting (**Figure 1A**). However, under similar casting conditions and settling tendencies the Mg—1Zr alloy exhibits better refinement, **Figure 1G** (Nagasivamuni et al., 2019a). This settling behavior of α-Zr particles alters the alloy composition and deviates from the intended alloy composition in the as-cast condition. After UST-L and UST-S, the amount of settling is reduced in the Mg—1Zr—AlBe alloy (**Figures 1B,C**), however, the grain refinement trend lies above the refinement produced by the Mg—1Zr alloy as shown in **Figure 1J**. The best refinement conditions for the Mg—1Zr—AlBe alloy can be expressed as UST-S > UST-L > as cast.

The composition analysis shown in **Table 1** is plotted in **Figure 1K** for Zr_T against Zr_S. A significant drop in Zr_S is noted for the Mg—1Zr—AlBe alloy with respect to Zr_T when compared to the Mg—1Zr alloy under all casting conditions. **Table 1** presents the amount of Zr_S in the alloy as a percentage with respect to the equilibrium solubility limit ($Zr_S = 0.5\ wt.\%$). A noticeable reduction is observed in the amount of Zr_S and this percent remains <20% (top region) after UST for the Mg—1Zr—AlBe alloy. It is well-known that Zr_S is responsible for the activation of α-Zr particles to achieve maximum grain refinement in Mg—Zr alloys (Qian and Das, 2006; Nagasivamuni et al., 2019a). Due to the very low solute content in the Mg—1Zr—AlBe alloy the extent of refinement is significantly lower for all casting conditions (**Figure 1J**).

Figures 2A,B show the microstructures from the bottom region of the as-cast Mg—1Zr and Mg—1Zr—AlBe alloys. Despite a high Zr_T (5.3%) and 0.33% Zr_S, it is interesting to note from **Figure 2B** that the grains in the Mg—1Zr—AlBe alloy are much larger (1550 ± 350 μm) than the grains observed in the Mg—1Zr alloy in this region (**Figure 2A** with 114 ± 38 μm). **Figures 2C,D** show the X-ray diffractogram of the particles present in the bottom region (**Figures 2A,B**) separated

TABLE 1 | Chemical analysis for Zr_S, Zr_T and percentage of solute in Mg−1Zr and Mg−1Zr−AlBe alloy under different casting conditions.

Alloy	Chemical analysis area	Casting condition	Analyzed composition in wt.%						Be (ppm)	Percentage of Zr_S*	Ref
			Zr_S	Zr_T	Al	Fe	Mn	Ti			
Mg−1Zr−AlBe	Top region	As-cast	0.019	0.053	0.075	<0.002	0.012	<0.002	<10	3.80	Present work
	Bottom region		0.330	5.350	0.043	0.009	0.014	0.08	82	66.0	
	Top region	UST-L	0.049	0.270	0.045	<0.002	0.006	<0.002	<10	9.80	
		UST-S	0.083	0.820	0.032	0.002	0.005	0.002	20	16.6	
Mg−1Zr	Top region	As-cast	0.250	0.300	0.004	<0.002	0.013	0.003	–	50.0	Nagasivamuni et al., 2019a
		UST-L	0.490	0.660	0.008	0.002	0.017	0.006	–	98.0	
		UST-S	0.410	0.990	0.010	0.002	0.012	0.007	–	80.0	

*Percentage of solute in the respective alloy is calculated by (Zr_S × 100)/0.5%.

for two ranges of 2θ to improve clarity. The base alloy contains predominantly Mg and Zr peaks. Due to their similar crystal structures most of the α—Zr coincides with α—Mg peaks. Since, the sample was taken from the bottom of the casting, crucible contamination such as Si peaks are identified.

Analysis of the particles in the Mg—1Zr—AlBe alloy were limited to binary phases of Zr containing Al and Be (ternary or multicomponent interactions were ignored). From **Figures 2C,D** it is observed that the intensity of prominent peaks of α–Zr at 36.68°, 57.42°, 68.69° and 90.48° in the Mg—1Zr alloy were lower for the Mg—1Zr—AlBe alloy. The possible combinations of Zr—Al phase are indicated in **Figure 2C** and other Zr-rich phases are marked as Zr_xAl_y because it is challenging to identify any specific Al—Zr phase at very low concentrations. A possible non-stoichiometric Zr—Al intermetallic compound is shown in **Figures 2C,D** because the addition of Mg—25Zr master alloy contains many α-Zr particles that can be easily affected by the dissolved Al atoms to form such phases. It should be noted at this stage (**Figure 2B**) that the interaction of Al with Zr has a tendency to decrease the excellent potency of Zr either by forming a different crystal structure or reducing the number of preferential planes for crystal nucleation on the surface of the α-Zr particles (Fan, 2013). **Figure 2B** shows a large increase in the particle size and α-Mg grain size which indicates significant growth or transformation of the α-Zr particles into Zr—Al phases. A slight enrichment of Be (0.0082%) is observed from the composition analysis in the bottom region, however, it is difficult to detect using X-ray analysis and to interpret its interaction.

Figure 3A shows the back scattered electron image of a grain (dashed line) with possible particles identified as nucleation sites (dotted circle) in the Mg—1Zr—AlBe alloy after UST-S. The elemental analysis of particles marked as A and B in **Figure 3A** are shown in **Figure 3B**. Both of these particles are rich in Zr with traces of Al. An enlarged view of Zr—Al particles in **Figure 3C** shows numerous small particles and few large white particles. The size distribution in **Figure 3D** shows that the particles present in UST-S and UST-L have an average size of $3.1 \pm 1.4\,\mu m$ and $2.8 \pm 2.0\,\mu m$, respectively. Very fine particles $<1\,\mu m$ were excluded from the analysis as they are unlikely to contribute to grain refinement (Greer et al., 2000). This size distribution of particles is slightly larger than that reported for the Mg—1Zr alloy (Nagasivamuni et al., 2019a) which might be due to the formation of Zr—Al phases. Elemental mapping in **Figure 3E** shows two types of Zr—Al particles with one rich in Zr and the other rich in Al based on relative color intensity. For a better understanding, individual particles and clusters of particles from the microstructure samples (middle region) were analyzed in different fields after UST-S and UST-L and the EDS analysis is shown in **Figures 3F,G**. It is found that almost all of the Zr nucleant particles were associated with the presence of Al. Considering the limitations due to SEM-EDS interaction volumes of, for example 1–5 microns, within the sample, it is almost impossible to find a Zr particle that does not contain Al. This indicates that most of the Al is concentrated toward the vicinity of the α-Zr particles. The ratio of normalized wt.% of Al/Zr reveals that the interaction of Al varies from a ratio as low as 0.2–0.5 indicating that most of the particles are rich in Zr and only a few particles are rich in Al. Therefore, it is observed that both Zr solute and Zr nucleant particles are affected by the addition of the Al—Be master alloy.

DISCUSSION

Significant grain coarsening was reported by Cao et al. (2004) in Zr containing and Zr-free Mg alloys and suggested that nucleant poisoning occurs due to a Be coating formed on the surface of potent particles because any excess addition of Zr to Be containing Mg—Zr alloy did not refine the grains. However, the interaction of Al with Zr or the amount of the dissolved solute Zr in the Be added alloy was not reported in detail. The results of the present work imply that Al is the cause of nucleant poisoning rather than Be. Because, it is well-documented that Be segregates to the surface of a magnesium melt forming either BeO (Zeng et al., 2001a; Horst and Barry, 2006) or a complex (Mg, Be)O layer (Tan et al., 2016, 2018), it is expected that most of the Be diffuses toward the surface of the melt where it is converted into protective oxides. The composition analysis in **Table 1** supports these observations because the Be concentration remaining in the bulk of the alloy is much lower (0.002%) than the intended composition (0.01%). Although the bottom (settled) region in the

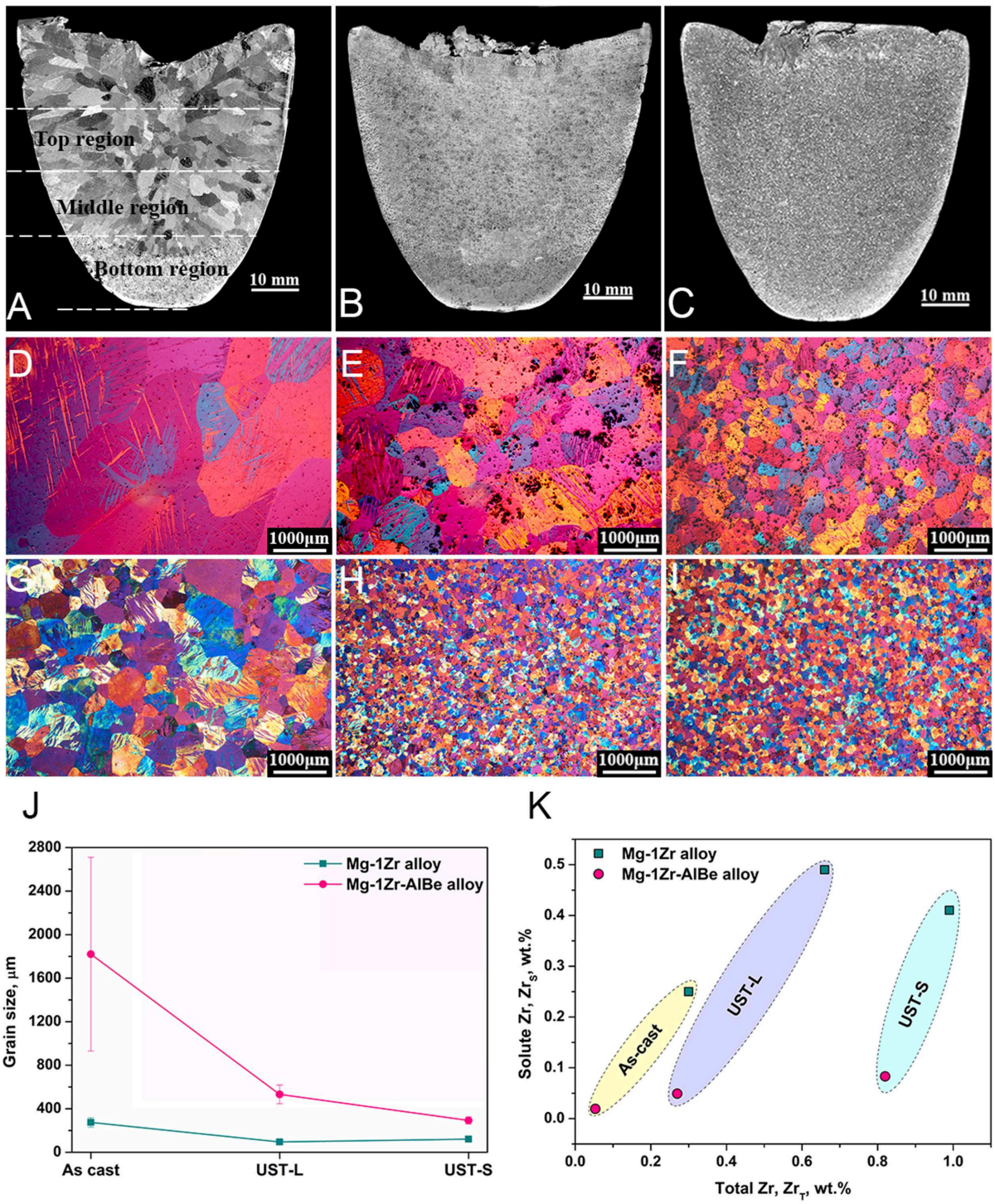

FIGURE 1 | Macrostructures of Mg—1Zr—AlBe alloy in **(A)** as-cast **(B)** UST-L and **(C)** UST-S conditions and their corresponding microstructures **(D–F)** were taken from the middle region of the casting. Under similar conditions the microstructures in **(G–I)** represent the Mg—1Zr alloy that shows excellent grain refinement. **(J)** Compares the grain size of the Mg—1Zr alloy with the Mg—1Zr—AlBe alloy. The inferior grain refinement performance is explained through the loss of solute Zr (Zr_S) plotted in **(K)**.

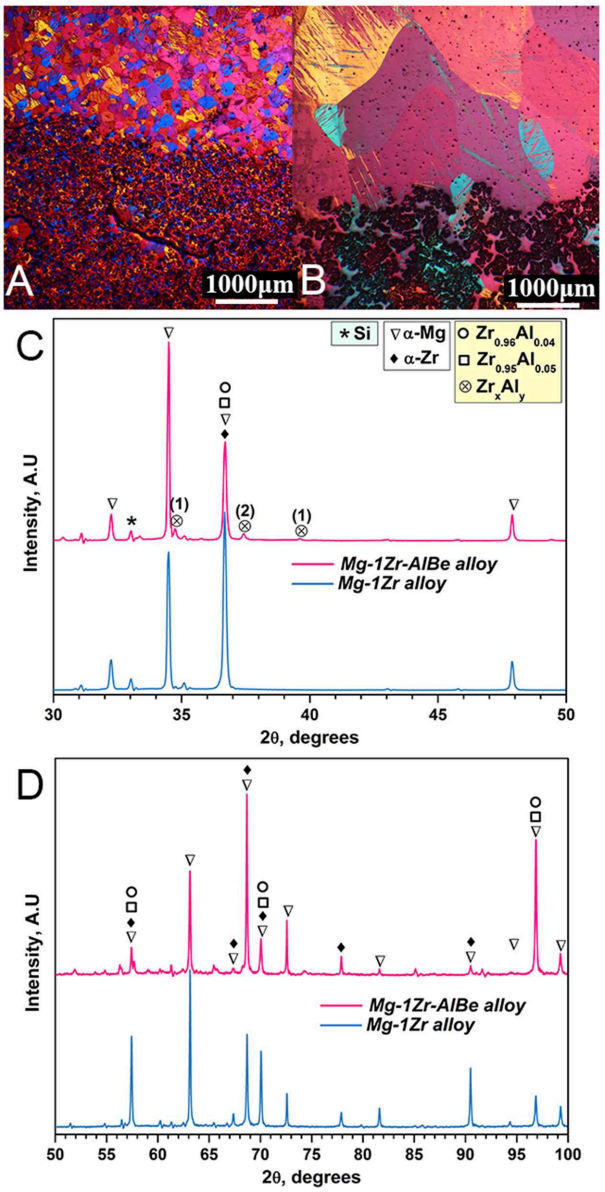

FIGURE 2 | Microstructures of as-cast **(A)** Mg—1Zr alloy and **(B)** Mg—1Zr—AlBe alloy analyzed from the bottom region of the casting exhibits different grain sizes due to the presence of potent and impotent particles (the black phase), respectively. Characterization of the Zr—Al intermetallic phases by an X-ray diffractogram of particles in the settled regions of **(A,B)**. To more clearly show the data the diffractogram is divided into the range of 2θ **(C)** from 30 to 50 degrees and **(D)** from 50 to 100 degrees.

as-cast Mg—1Zr—AlBe alloy contains 0.0082% Be, after UST-S with a reduced settling effect (**Figure 1C**) the Be concentration in the melt is only 0.0002%. The percentage ratio of Be/Zr_T essentially remains the same at 0.15% and 0.24% in as-cast and after UST-S. Therefore, the interaction of Be with Zr nucleant particles can be considered to be insignificant when compared to the effect of Al. Regarding the interaction of Be with the native nucleant particles, a grain coarsening tendency is reported as being more noticeable in commercial purity Mg than in high purity ingot (Ichikawa and Saito, 1963) and Be addition is also patented as a powerful Fe removal agent for Mg alloys (Cao et al., 2004; StJohn et al., 2005). Because the mechanism of the Fe/Mn interaction with nucleant particles is not known in Zr-free Mg alloys (StJohn et al., 2005, 2013), the grain coarsening effect of Be in those alloys needs further research.

The dissolved Al which is at a higher concentration (0.2 wt.%) than Be (0.01%), interacts with Zr in two possible ways (i) with undissolved α-Zr particles and (ii) with dissolved Zr present as solute (Zr_S). **Table 2** lists the possible Zr—Al phases reported for an equilibrium Al—Mg—Zr system after (Bochvar and Bulanova, 2005) in which it is stated that at least 0.05 % Al and 0.04 % Zr is required for the formation of $ZrAl_3$. For Al concentrations below this limit intermetallic precipitates such as Zr_2Al, Zr_2Al_3, Zr_4Al_3, and Zr rich phases are probable as shown in XRD analysis (**Figure 2C**). To compare with the chemical analysis results estimated in wt.%, the fraction of Al, Zr and the Al/Zr ratio were calculated from the molecular weight of individual intermetallic phases. The fraction of Al/Zr estimated from the normalized wt.% of EDS analysis is also included in **Table 2** where it matches with the Al/Zr ratio of some of the possible Zr—Al phases. It should be noted that this normalized wt.% from the EDS analysis is based on the concentration of elements present in that region regardless of the type of crystalline phase. Therefore, EDS quantification cannot be directly approximated for the characterization of a particular intermetallic phase.

From **Table 1**, it is found that UST can increase the amount of solute Zr to the maximum solubility level of 0.5 wt.% in the Mg—1Zr alloy. Therefore, the precipitation of the Zr—Al intermetallic phases was assumed to occur from both dissolved Al (0.2 wt.%) and solute Zr (0.5 wt.%) and the corresponding amount (in wt.%) of different Zr—Al phases are calculated by taking Al as the reaction limiting element and presented in **Table 2**. From **Table 2**, it is interesting to note that formation of one or more combinations of Zr—Al phases could lead to severe loss of both Zr as solute and total Zr in the alloy. For instance, if it is assumed that only $ZrAl_3$ intermetallic is formed in the melt because this intermetallic phase is often found in Mg—Zr alloys that contain Al (Lavernia et al., 1987; Fan, 2013), then the Mg—1Zr—AlBe alloy is still left with free solute of 0.3 wt.% Zr and total Zr of 0.8 wt.%. This level of solute Zr and unaffected α-Zr particles are sufficient to obtain significant refinement (Nagasivamuni et al., 2019a). However, in Mg alloys containing (3–10 wt.%) Al and (0.01–1.6 wt.%) Zr (Bochvar and Bulanova, 2005) and in AZ91 alloy (Kabirian and Mahmudi, 2009), $ZrAl_2$ and Zr_2Al_3 were identified and no $ZrAl_3$ phase was reported. According to **Table 2**, the formation of $ZrAl_2$ and Zr_2Al_3 could almost deplete the amount of solute Zr present in Mg—1Zr alloy (consuming 50% of total Zr). For even richer Zr phases (Al/Zr $<$ 0.30) such as Zr_4Al_3 and Zr_3Al_2, complete consumption of Zr occurs and the melt is left with only impotent nucleation substrates of Zr—Al particles. For instance, the formation of tetragonal $ZrAl_3$ phase has a lattice misfit of 12.55% with α—Mg compared to potent α—Zr particles with a misfit of only 0.67% (Fan, 2013). Interestingly, the values of Zr_S and Zr_T become negative if one

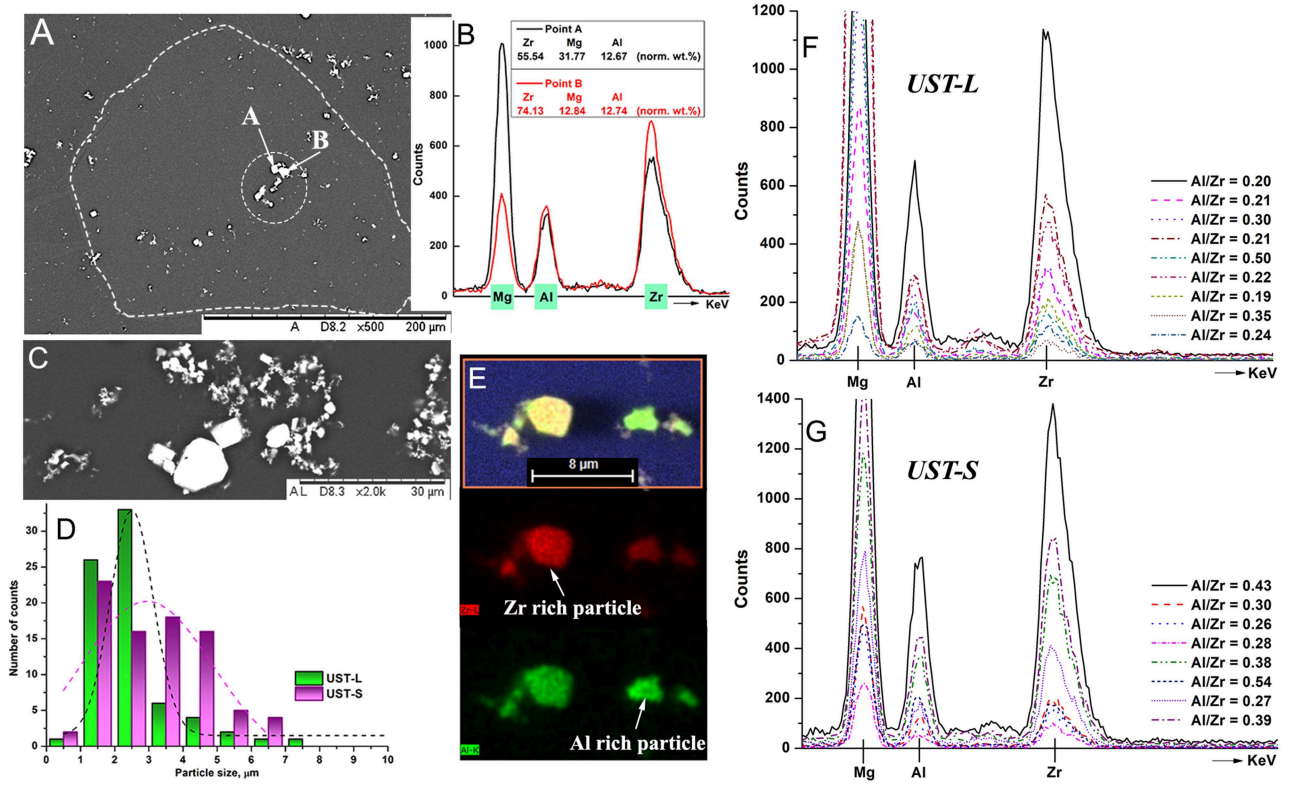

FIGURE 3 | (A) Back scattered electron image of Mg—1Zr—AlBe alloy after UST-S showing a grain within the dashed line and possible nucleant particles are denoted as A and B. **(B)** shows the corresponding EDS analysis. **(C)** BSD image of particles with different sizes and **(D)** shows their size distribution histograms. Two types of Zr—Al particles were identified in **(E)** with one rich in Zr and the another particle rich in Al. Almost all the α-Zr particles contain Al in **(F)** UST-L and **(G)** UST-S conditions where the Al/Zr ratio varies between 0.2 and 0.5 calculated from normalized wt.%.

TABLE 2 | Quantification of possible binary Zr—Al intermetallic phases according to the Al—Mg—Zr equilibrium diagrams (Bochvar and Bulanova, 2005) and from the XRD database.

Phases	Fraction of Al and Zr in each phase (calculated from molecular wt.%)			Al/Zr fraction from EDS measurements (norm. wt.%)	Al as rate limiting element[a]	Amount of Zr-Al phases formed[b]	Amount of Zr needed	Free solute Zr available[c]	Total Zr left unaffected[d]
	Al	Zr	Al/Zr	(wt.%)	(wt.%)	(wt.%)	(wt.%)	(wt.%)	(wt.%)
$ZrAl_3$	0.4701	0.5298	0.8873	–	0.19	0.42	0.22	0.27	0.77
$ZrAl_2$	0.3716	0.6283	0.5915	0.50–0.54	0.20	0.54	0.34	0.16	0.66
Zr_2Al_3	0.3073	0.6926	0.4436	0.26–0.43	0.19	0.65	0.45	0.05	0.54
ZrAl	0.2282	0.7717	0.2957		0.19	0.85	0.65	–0.15	0.34
Zr_4Al_3	0.1815	0.8184	0.2218		0.19	1.10	0.90	–0.40	0.09
Zr_3Al_2	0.1647	0.8352	0.1971	0.19–0.24	0.19	1.20	1.00	–0.50	0.00
Zr_5Al_3	0.1507	0.8492	0.1774		0.19	1.30	1.10	–0.60	–0.10
Zr_2Al	0.1288	0.8711	0.1478	–	0.19	1.55	1.35	–0.85	–0.35
Zr_3Al	0.0897	0.9102	0.0985	–	0.19	2.20	2.00	–1.50	–1.00
$Zr_{0.95}Al_{0.05}$	0.0153	0.9846	0.0155	–	0.20	13.0	12.80	–12.3	–11.80
$Zr_{0.96}Al_{0.04}$	0.0121	0.9878	0.0123	–	0.20	16.4	16.20	–15.7	–15.20

[a] *Addition of Al—Be master alloy increases the Al concentration in the melt to 0.2 wt.% max.*
[b] *Amount of Zr—Al phases are calculated by assuming that all dissolved Al is consumed to form the particular intermetallic phase.*
[c] *Free solute Zr left in the Mg—1Zr alloy calculated from the equilibrium solute content of 0.5 wt.%.*
[d] *Calculated from the total Zr (1.0 wt.%).*

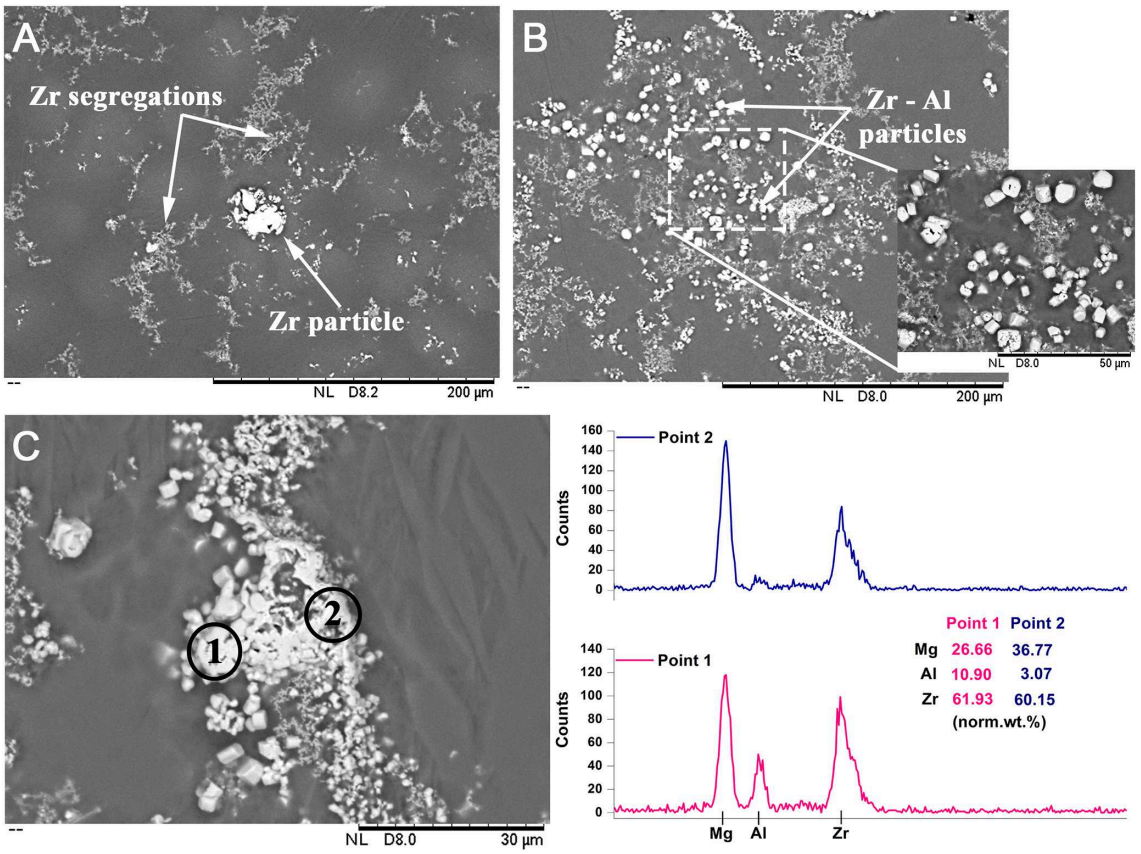

FIGURE 4 | BSD images of **(A)** the as-cast Mg—1Zr alloy showing the presence of a blocky undissolved α-Zr particle and fine Zr particle segregation and **(B)** the Mg—1Zr—AlBe alloy showing faceted Zr—Al intermetallic particles. **(C)** BSD image of a Zr particle cluster in the Mg—1Zr—AlBe alloy surrounded by fine precipitates of Zr—Al intermetallic phases. EDS analysis shows that point 1 contains Al and Zr, whereas point 2 is rich in Zr.

or more combinations of Zr rich phases occurs in the melt consuming all the Zr added to the alloy. It should be noted that the formation of more Zr-rich phases at very low concentrations of Al can consume 2–16% of Zr and this explains the important reason why any excess addition of Zr to Mg alloys containing Al is not effective in promoting significant grain refinement. The calculation indicates that most of the Zr—Al constituents in **Table 2** fall below 2% therefore, no strong peak was observed in the XRD graph to characterize a particular intermetallic other than α—Zr, $Zr_{0.95}Al_{0.05}$, and $Zr_{0.96}Al_{0.04}$. Although some possible phases based on the high intensity lines were characterized as Zr_3Al_2 and Zr_5Al_3 marked as 1 and 2, respectively in **Figure 2C**, which also matches closely with the EDS and chemical analysis results of Zr_S.

It should be noted that the above discussion is based on the assumption that dissolved Al and solute Zr results in Zr—Al phase formation. However, in order to form a Zr—Al intermetallic from dissolved constituents, a substrate is needed to facilitate nucleation and growth (Wang et al., 2017a). In the case of the Mg—1Zr—AlBe alloy, the melt initially contains numerous α-Zr particles that could readily serve as nucleation sites for the Zr—Al phases. Therefore, it is necessary to understand the interaction of the dissolved Al with undissolved α-Zr particles in the melt. **Figures 4A,B** show the BSD image of the Mg—1Zr and Mg—1Zr—AlBe alloys from the bottom region in the as-cast condition. **Figure 4A** shows Zr as bands of fine particles segregated along the grain boundary regions and a larger undissolved α-Zr particle with an approximate size of ∼25 µm. After the addition of Al—Be master alloy, several Zr—Al particles are observed within the Zr segregated regions and these particles are distinctly identified as faceted structures. The magnified insert image in **Figure 4B** shows these Zr—Al intermetallic particles more clearly. **Figure 4C** shows a typical cluster of α-Zr particles in the Mg—1Zr—AlBe alloy. EDS analysis at point 1 shows the presence of Al and Zr while at point 2 the cluster is rich in Zr with very low Al. This might be a larger Zr particle similar to that shown in **Figure 4A**, which is surrounded by numerous fine Zr—Al phases after the addition of the Al—Be master alloy. Therefore, it is more likely that the α-Zr particles act as preferential heterogeneous sites for the precipitation of fine Zr—Al phases in the melt which are then dispersed into the melt. The precipitation and growth of Zr – Al phases would lead to the significant reduction in the solute Zr content observed in the alloy. These observations would explain the coarse grain size

(1.55 mm) observed in the bottom region of the as-cast Mg—1Zr—AlBe alloy that contains 5.3 wt.% of particles (**Figure 2B**) where the growth restriction factor of the alloy is now very low and the distance between potent particles is also very large.

The liquid treatment, UST-L, produces excellent refinement when the alloy contains more potent substrates and solute (Atamanenko et al., 2010; Wang et al., 2017c; Nagasivamuni et al., 2019a). The solidification treatment UST-S, on the other hand, can produce refinement in pure metals (Wang et al., 2017d; Nagasivamuni et al., 2018) and dilute alloys (Wang et al., 2014, 2016a, 2017b; Srivastava et al., 2017) without potent substrates. The mechanism of refinement in both cases is briefly explained elsewhere (Nagasivamuni et al., 2018, 2019a,b). UST-L produces a better dispersion of particles than the as-cast condition, however, the activation of nucleation depends on the amount of solute (Zr_S) in the alloy. During UST-S, nucleation is favored by forced acoustic convection and low temperature gradients (Wang et al., 2017b; Nagasivamuni et al., 2018, 2019a,b). It is interesting to note that in either case, the presence of solute plays an important role in facilitating nucleation and the survival of grains which can be understood by comparison with the Mg—1Zr alloy (**Figure 1J**). Due to the poisoning of the α-Zr particles and the low amount of Zr solute, the extent of grain refinement is less than that of the Mg—1Zr alloy. Nevertheless, UST demonstrates the potential to refine the grains in the alloy containing low additions of Al and Be and could be beneficial for the development of ignition resistant and grain refined Mg alloys.

CONCLUSIONS

This research reveals that the grain coarsening effect of the Al—Be master alloy added to a Mg—Zr alloy mainly arises from the interaction of Al and Zr resulting in the formation of Al—Zr intermetallic phases and a reduction in the amount of Zr solute rather than an effect of Be. Together, the reduction in potency of α-Zr particles as nucleants and the amount of Zr solute due to reaction with Al cause grain coarsening. The significantly lower concentration of Be in the cast and UST processed alloy (<0.001 and 0.002%, respectively) supports the results of other research that Be has diffused to the surface of the melt forming oxides. Even at very low Zr solute contents and with impotent Zr nucleant particles, UST-S produces a greater reduction in grain size than produced by UST-L, demonstrating the potential to develop ignition proof, grain refined Mg castings with Be addition.

DATA AVAILABILITY STATEMENT

All datasets generated for this study are included in the article/supplementary material.

AUTHOR CONTRIBUTIONS

NB designed and performed the experiments, analyzed, characterized the results, designed the figures, and drafted the manuscript. GW and MD supervise the findings of the work and contributed to the final version of manuscript by evaluating the methods and procedures adopted in nucleant particle characterization. DS critically reviewed the concepts of discussion, characterization, interpretation of the results, and significantly contributed to improving the writing of the manuscript. All the authors contributed to the results and discussion section of the manuscript.

FUNDING

The authors acknowledge the funding support provided by Australian Research Council Research Hub for Advanced Manufacturing of Medical Devices IH150100024, the ARC Discovery grant DP140100702 and ARC linkage project LP150100950.

ACKNOWLEDGMENTS

NB thanks Qiyang Tan for provision of the Al—5Be master alloy. The authors also thank the scientific and technical assistance of the Australian Microscopy and Microanalysis Research Facility at the Center for Microscopy and Microanalysis, The University of Queensland.

REFERENCES

Atamanenko, T. V., Eskin, D. G., Zhang, L., and Katgerman, L. (2010). Criteria of grain refinement induced by ultrasonic melt treatment of aluminum alloys containing Zr and Ti. *Metallurgical Mater.Trans A.* 41, 2056–2066. doi: 10.1007/s11661-010-0232-4

Bochvar, N. R., and Bulanova, M. V. (2005). "Al-Mg-Zr (Aluminium - Magnesium - Zirconium): datasheet from landolt-börnstein - group IV physical chemistry volume 11A3," in *Light Metal Systems. Part 3* eds G. Effenberg and S. Ilyenko (Berlin, Heidelberg: SpringerMaterials; Springer-Verlag).

Cao, P., Qian, M., and StJohn, D. H. (2004). Grain coarsening of magnesium alloys by beryllium. *Scr. Mater.* 51, 647–651. doi: 10.1016/j.scriptamat.2004.06.022

Czerwinski, F. (2014). Controlling the ignition and flammability of magnesium for aerospace applications. *Corros. Sci.* 86, 1–16. doi: 10.1016/j.corsci.2014.04.047

Du, J., Wang, M. H., and Li, W. F. (2010). Effects of Fe addition and addition sequence on carbon inoculation of Mg-3%Al alloy. *J. Alloys Compd.* 502, 74–79. doi: 10.1016/j.jallcom.2010.04.156

Easton, M. A., Schiffl, A., Yao, J. Y., and Kaufmann, H. (2006). Grain refinement of Mg-Al(-Mn) alloys by SiC additions. *Scr. Mater.* 55, 379–382. doi: 10.1016/j.scriptamat.2006.04.014

Eskin, D. G. (2014). Ultrasonic melt processing: opportunities and misconceptions. *Aluminium Alloys* 2014 - ICAA14 794–796, 101–106. doi: 10.4028/www.scientific.net/MSF.794-796.101

Eskin, D. G. (2017). Ultrasonic processing of molten and solidifying aluminium alloys: overview and outlook. *Mater. Sci. Technol.* 33, 636–645. doi: 10.1080/02670836.2016.1162415

Fan, Z. (2013). An epitaxial model for heterogeneous nucleation on potent substrates. *Metall. Mater Trans. A* 44, 1409–1418. doi: 10.1007/s11661-012-1495-8

Greer, A. L., Bunn, A. M., Tronche, A., Evans, P. V., and Bristow, D. J. (2000). Modelling of inoculation of metallic melts: application to grain refinement of aluminium by Al-Ti-B. *Acta Mater.* 48, 2823–2835. doi: 10.1016/S1359-6454(00)00094-X

Horst, F. E., and Barry, M. L. (ed.). (2006). "Magnesium casting alloys," in *Magnesium Technology: Metallurgy, Design Data, Applications* (Berlin, Heidelberg: Springer Berlin Heidelberg), 145–218.

Huang, Y. D., Zheng, X. H., Kainer, K. U., and Hort, N. (2010). "Mechanism of grain refinement in Mg-Al alloys with carbon inoculations," in *New Frontiers in Light Metals: Proceedings of the 11th International Aluminium Conference INALCO 2010*, eds. L. Katgerman and F. Soetens (IOS Press), 451–460. doi: 10.3233/978-1-60750-586-0-451

Ichikawa, R., and Saito, R. (1963). The distribution of Be and the grain size on Mg-Al alloys containing Be. *J. Jpn Inst Metals* 27, 32–37. doi: 10.2320/jinstmet1952.27.1_32

Kabirian, F., and Mahmudi, R. (2009). Effects of zirconium additions on the microstructure of As-cast and aged AZ91 magnesium alloy. *Adv. Eng. Mater.* 11, 189–193. doi: 10.1002/adem.200800223

Lavernia, E. J., Gomez, E., and Grant, N. J. (1987). The structures and properties of Mg-Al-Zr and Mg-Zn-Zr alloys produced by liquid dynamic compaction. *Mater. Sci. Eng.* 95, 225–236. doi: 10.1016/0025-5416(87)90514-3

Nagasivamuni, B., Wang, G., StJohn, D. H., and Dargusch, M. S. (2018). The effect of ultrasonic treatment on the mechanisms of grain formation in as-cast high purity zinc. *J. Cryst. Growth* 495, 20–28. doi: 10.1016/j.jcrysgro.2018.05.006

Nagasivamuni, B., Wang, G., StJohn, D. H., and Dargusch, M. S. (2019a). Effect of ultrasonic treatment on the alloying and grain refinement efficiency of a Mg – Zr master alloy added to magnesium at hypo- and hyper-peritectic compositions. *J. Cryst. Growth* 512, 20–32. doi: 10.1016/j.jcrysgro.2019.02.004

Nagasivamuni, B., Wang, G., StJohn, D. H., and Dargusch, M. S. (2019b). *Mechanisms of Grain Formation During Ultrasonic Solidification of Commercial Purity Magnesium*. Springer International Publishing. 1579–1586.

Nimityongskul, S., Jones, M., Choi, H., Lakes, R., Kou, S., and Li, X. C. (2010). Grain refining mechanisms in Mg-Al alloys with Al4C3 microparticles. *Mater. Sci. Eng. A* 527, 2104–2111. doi: 10.1016/j.msea.2009.12.030

Qian, M., and Das, A. (2006). Grain refinement of magnesium alloys by zirconium: formation of equiaxed grains. *Scr. Mater.* 54, 881–886. doi: 10.1016/j.scriptamat.2005.11.002

Qian, M., Ramirez, A., Das, A., and StJohn, D. H. (2010). The effect of solute on ultrasonic grain refinement of magnesium alloys. *J. Cryst. Growth* 312, 2267–2272. doi: 10.1016/j.jcrysgro.2010.04.035

Qian, M., StJohn, D. H., and Frost, M. T. (2003). Effect of soluble and insoluble zirconium on the grain refinement of magnesium alloys. *Magnesium Alloys 2003* 419–4, 593–598. doi: 10.4028/www.scientific.net/MSF.419-422.593

Ramirez, A., Qian, M., Davis, B., Wilks, T., and StJohn, D. H. (2008). Potency of high-intensity ultrasonic treatment for grain refinement of magnesium alloys. *Scr. Mater.* 59, 19–22. doi: 10.1016/j.scriptamat.2008.02.017

Sreekumar, V. M., and Eskin, D. G. (2016). A new Al-Zr-Ti master alloy for ultrasonic grain refinement of wrought and foundry aluminum alloys. *Jom* 68, 3088–3093. doi: 10.1007/s11837-016-2120-x

Srivastava, N., Chaudhari, G. P., and Qian, M. (2017). Grain refinement of binary Al-Si, Al-Cu and Al-Ni alloys by ultrasonication. *J. Mater. Process. Technol.* 249, 367–378. doi: 10.1016/j.jmatprotec.2017.06.024

StJohn, D. H., Easton, M. A., Qian, M., and Taylor, J. A. (2013). Grain refinement of magnesium alloys: a review of recent research, theoretical developments, and their application. *Metall. Mater. Trans. A* 44a, 2935–2949. doi: 10.1007/s11661-012-1513-x

StJohn, D. H., Qian, M., Easton, M. A., Cao, P., and Hildebrand, Z. (2005). Grain refinement of magnesium alloys. *Metall. Mater. Trans. A* 36a, 1669–1679. doi: 10.1007/s11661-005-0030-6

Tan, Q. Y., Mo, N., Jiang, B., Pan, F. S., Atrens, A., and Zhang, M. X. (2016). Oxidation resistance of Mg-9Al-1Zn alloys micro-alloyed with Be. *Scr. Mater.* 115, 38–41. doi: 10.1016/j.scriptamat.2015.12.022

Tan, Q. Y., Mo, N., Lin, C. L., Jiang, B., Pan, F. S., Huang, H., et al. (2018). Improved oxidation resistance of Mg-9Al-1Zn alloy microalloyed with 60 wt ppm Be attributed to the formation of a more protective (Mg,Be)O surface oxide. *Corros. Sci.* 132, 272–283. doi: 10.1016/j.corsci.2018.01.006

Wang, E. Q., Wang, G., Dargusch, M. S., Qian, M., Eskin, D. G., and StJohn, D. H. (2016a). Grain refinement of an Al-2 wt%Cu alloy by Al3Ti1B master alloy and ultrasonic treatment. *IOP Conf. Ser.* 117:012050. doi: 10.1088/1757-899X/117/1/012050

Wang, F., Eskin, D., Connolley, T., and Mi, J. W. (2017a). Influence of ultrasonic treatment on formation of primary Al3Zr in Al—0.4Zr alloy. *Trans. Nonferrous Met. Soc. China* 27, 977–985. doi: 10.1016/S1003-6326(17)60115-8

Wang, G., Croaker, P., Dargusch, M., McGuckin, D., and StJohn, D. (2017b). Simulation of convective flow and thermal conditions during ultrasonic treatment of an Al-2Cu alloy. *Comput. Mater. Sci.* 134, 116–125. doi: 10.1016/j.commatsci.2017.03.041

Wang, G., Dargusch, M. S., Eskin, D. G., and StJohn, D. H. (2017c). Identifying the stages during ultrasonic processing that reduce the grain size of aluminum with added Al3Ti1B master alloy. *Adv. Eng. Mater.* 19:1700264. doi: 10.1002/adem.201700264

Wang, G., Dargusch, M. S., Qian, M., Eskin, D. G., and StJohn, D. H. (2014). The role of ultrasonic treatment in refining the as-cast grain structure during the solidification of an Al-2Cu alloy. *J. Cryst. Growth* 408, 119–124. doi: 10.1016/j.jcrysgro.2014.09.018

Wang, G., Qiang Wang, E., Prasad, A., Dargusch, M., and StJohn, D. H. (2016b). "Grain refinement Of Al-Si hypoeutectic alloys By Al3Ti1B master alloy and ultrasonic treatment," in *Shape Casting: 6th International Symposium*. John Wiley & Sons, Inc., 141–150.

Wang, G., Wang, Q., Easton, M. A., Dargusch, M. S., Qian, M., Eskin, D. G., et al. (2017d). Role of ultrasonic treatment, inoculation and solute in the grain refinement of commercial purity aluminium. *Sci. Rep.* 7:9729. doi: 10.1038/s41598-017-10354-6

Zeng, X. Q., Wang, Q. D., Lu, Y. H., Ding, W. J., Zhu, Y. P., Zhai, C. Q., et al. (2001a). Behavior of surface oxidation on molten Mg-9Al-0.5Zn-0.3Be alloy. *Mater. Sci. Eng. A* 301, 154–161. doi: 10.1016/S0921-5093(00)01798-6

Zeng, X. Q., Wang, Q. D., Lu, Y. Z., Zhu, Y. P., Ding, W. J., and Zhao, Y. H. (2001b). Influence of beryllium and rare earth additions on ignition-proof magnesium alloys. *J. Mater. Process. Technol.* 112, 17–23. doi: 10.1016/S0924-0136(00)00854-2

Conflict of Interest: The authors declare that the research was conducted in the absence of any commercial or financial relationships that could be construed as a potential conflict of interest.